RESEARCH ARTICLE

RF-EMF Exposure Assessment of Fetus During the First Trimester of Pregnancy

SRIKUMAR SANDEEP[1], ALIREZA VARD[1,2], MÒNICA GUXENS[3,4,5,6], ISABELLE BLOCH[1,7], AND JOE WIART[1], (Senior Member, IEEE)

[1]LTCI, Télécom Paris, Institut Polytechnique de Paris, 91120 Palaiseau, France
[2]Department of Bioelectrics and Biomedical Engineering, School of Advanced Technologies in Medicine, Isfahan University of Medical Sciences, Isfahan 81746, Iran
[3]ISGlobal, 08036 Barcelona, Spain
[4]Department of Medicine and Life Sciences, Universitat Pompeu Fabra, 08002 Barcelona, Spain
[5]Spanish Consortium for Research on Epidemiology and Public Health (CIBERESP), Instituto de Salud Carlos III, 28029 Madrid, Spain
[6]Department of Child and Adolescent Psychiatry/Psychology, Erasmus University Medical Centre, 3015 GD Rotterdam, The Netherlands
[7]Sorbonne Université, CNRS, LIP6, 75006 Paris, France

Corresponding author: Isabelle Bloch (isabelle.bloch@sorbonne-universite.fr)

ABSTRACT This article describes the computational analysis of Radio Frequency - Electromagnetic Field (RF-EMF) exposure of Uterus-Fetus Units (UFUs) embedded inside the body of a 26 year old human female. Realistic UFU models are obtained from ultrasound images acquired for different fetuses and at specific development stages (7 weeks, 9 weeks and 11 weeks old), for which a deep-learning based segmentation method is developed. Each UFU model is then inserted into a computational electromagnetic model of a 26 year old female. The Specific Absorption Rate (SAR) of the fetus at commonly used wireless communication frequencies is estimated using a commercially available numerical electromagnetic solver. The Inverted F antenna (IFA), which is a commonly used mobile phone antenna was used as the excitation source. Fetus SAR values are reported for different combinations of excitation frequencies, phone positions and UFU ages. It was found that the fetus SAR for all the cases is well below the maximum allowable exposure limit of 80 mW/kg, as prescribed by ICNIRP. Furthermore, we replaced the embryo with uterus tissues and calculated the SAR in the uterus tissues (i.e. uterus tissues with same volume and shape, and at the same location as that of UFU). The uterus SAR values were found to be only marginally different from that of fetus SAR.

INDEX TERMS Dosimetry, fetus, RF exposure, SAR, ultrasound, image segmentation, deep learning.

I. INTRODUCTION

With the increasing use of wireless communication technologies in everyday life, there is a public concern about the possible adverse health impact linked to electromagnetic field exposure. The main concern in Radio Frequency - ElectroMagnetic Field (RF-EMF) exposure [1] is the energy

The associate editor coordinating the review of this manuscript and approving it for publication was Valerio De Santis.

deposited in the biological tissues. Biological tissues are electrically lossy materials characterized by non-zero conductivity or non-zero imaginary part of permittivity. The electromagnetic energy absorbed by these lossy tissues is converted to heat energy. The absorbed EM energy is quantified by the Specific Absorption Rate (SAR). SAR is the power absorbed per unit and is defined as:

$$\text{SAR} = \frac{\sigma(\bar{r})|\bar{E}(\bar{r})|^2}{2\rho(\bar{r})} \ (\text{W/kg}) \qquad (1)$$

where σ (Sm^{-1}) is the electrical conductivity, ρ (kgm^{-3}) is the mass density, $\bar{E}$ (Vm^{-1}) is the electric field intensity vector in the frequency domain and $\bar{r}$ is the position vector.

Recently, several computational studies were proposed for estimating the RF-EMF exposure in a plethora of cases [2], [3], [4], [5], [6], [7], [8], [9], [10], [11], [12]. In particular, the correlation between RF-EMF exposure and embryo and fetal development at different stages of gestation is of interest. The World Health Organization (WHO) identified fetal exposure as of high priority [13]. Previous works on fetal RF-EMF exposure can be classified according to the excitation sources (i.e. plane wave, cell phone, Magnetic Resonance Imaging (MRI) field, etc.), frequency, embryo age, and uterus-fetus unit (UFU) model creation procedures. Some of the initial works involved exposure analysis of pregnant women with fetus embedded for the case of an incident plane wave [5], [6], [7]. Plane wave excitation can be used only when the human body is in the far-field of the radiating source. In addition to the limitation of using a plane wave, Kawai et. al. [6] used simple geometries such as cube and spheroidal shapes to approximate the embryo. Fetus whole body SAR (WBSAR) and fetus brain SAR for the case of a plane wave at 2100 MHz were reported in [7]. In [7], the 8 to 13 weeks old UFU models were obtained from segmentation of ultrasound images, and 14 to 32 weeks UFU models were generated from MRI images and fetus growth modeling tools. Furthermore, a truncated model of a pregnant woman was used to limit the simulation resources. In comparison to [7], our work uses a full female body for simulation.

In a more recent work [4], stochastic dosimetry was used to assess the fetal exposure for the case of a 4G Long Term Evolution (LTE) tablet. The authors of [4] used a generic model based on MRI images for developing the 3-month UFU and the 9-month UFU was a scaled female baby. Some of the other noteworthy works include [8], [9], [10], [11]. In these papers, temperature elevation and SAR changes in the tissues of pregnant woman and fetus during MRI procedure was reported. However, the results were for MRI frequencies of 64 MHz and 128 MHz.

In this paper, we analyse RF-EMF exposure at different stages of UFU development at the end of the first trimester of pregnancy. We consider UFUs of three different ages: 7 weeks, 9 weeks and 11 weeks. Using ultrasound (US) data, we develop 3D computational models of embryos at these three stages of pregnancy. Ultrasound data were used since MRI procedure is not recommended in early stage pregnancy. The UFU models are then inserted into a numerical electromagnetic model of a non-pregnant adult female. This is followed by simulations to predict the fetus SAR. The fetus SAR is calculated at commonly used wireless communication frequencies. The frequencies used in this work are 1800 MHz, 2100 MHz, 2400 MHz, 2600 MHz and 3500 MHz. Our work is unique in the sense that we deal with early stage embryos of 7 weeks, 9 weeks and 11 weeks old, which contrasts with the older embryos aged 3 months and 9 months studied in [4]. Furthermore, while deformation of female human belly to insert larger embryos was done in [4], [7], since the size of embryos used in our work is smaller, it was not necessary to deform the female human model.

The paper outline is as follows. For the sake of clarity the method is divided into its main steps, each described in a separate section. In Section II, we describe the image segmentation of ultrasound data using deep learning techniques. In Section III, details of the computational electromagnetic modeling is provided. This is followed by cell phone antenna design and SAR assessment procedure in Section IV. Simulation results and conclusions are provided in Section V and Section VI, respectively.

## II. SEGMENTATION OF UTERUS AND FETUS IN ULTRASOUND IMAGES

The first step consists in building realistic digital 3D models of fetus from the segmentation of ultrasound images. Data were collected as part of the Generation R Next Study, and provided by the Generation R Study Group, Erasmus University Medical Center Rotterdam, in accordance with the Dutch Data Protection Act and the EU Directive 95/46/EC.

We employed the U-Net model [14] to segment the uterus and fetus in ultrasound images. As one of the most popular deep-learning methods for image segmentation, U-Net has demonstrated state of the art results in several applications [15], [16], [17], and was applied successfully on ultrasound images [18], [19], [20], including fetal segmentation [21], [22], [23]. In this section, we describe the image data preparation, model architecture and implementation, as well as a Graphical User Interface (GUI) that facilitates the usage of the proposed method.

A. IMAGE DATA PREPARATION

Since manual segmentation and labeling is a tedious task, we propose an iterative method, where the network trained at one step is used to segment more images, and is then retrained after correction of these segmentations. An initial data set contains 12 sequences of US images obtained at different stages of pregnancy, including two cases at 7 weeks of pregnancy, five cases at 9 weeks of pregnancy, and five cases at 11 weeks of pregnancy. In total, 1376 2D images were obtained from these 12 sequences. The uterus and fetus regions were manually segmented in each image, and mask images corresponding to them were produced, defining the reference used for training and evaluation. Our model was trained with this dataset.

Then new cases were segmented using this trained network, which is a fast process. Manual corrections were then done when needed, which is far less time consuming than doing the complete segmentation manually. These images and their corrected segmentations were then used to increase the dataset and to retrain the model to improve performance. This procedure was iterated a few times (6 with our actual dataset). At the end of this process, the final model was trained by using 69 sequences of US images (12 cases at
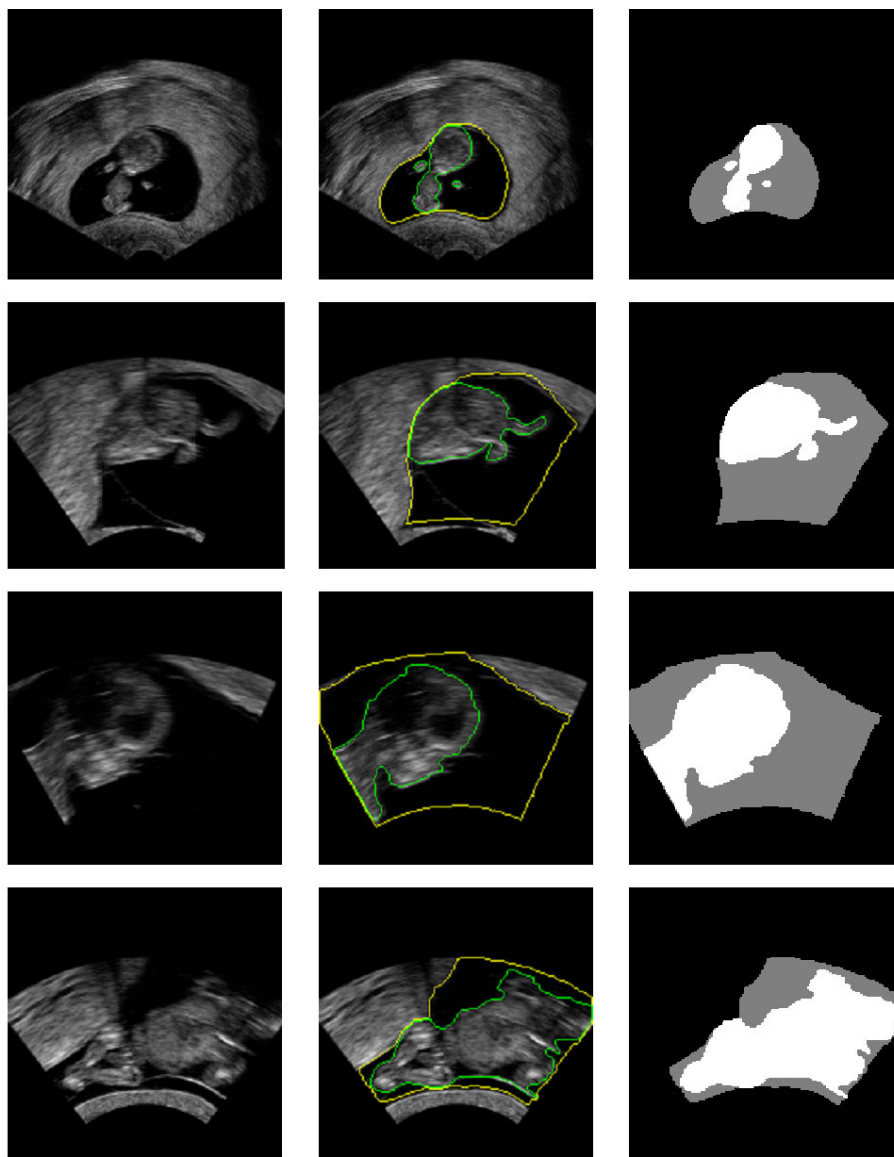
FIGURE 1. Examples of data used in this study. Column 1: Original US images. Column 2: Manual segmentations corresponding to Column 1. Column 3: Labeled masks (white: fetus, gray: uterus).

7 weeks of pregnancy, 22 cases at 9 weeks of pregnancy, and 35 cases at 11 weeks) with a total of 4974 2D images, which significantly improved the results of segmentation.

To guarantee that no bias was introduced by this procedure, the final network was tested on images not seen at all during training, and the results were evaluated visually, as well as quantitatively using the Dice index. Figure 1 shows some original US images selected from our dataset and their corresponding manual segmentations and masks.

B. MODEL ARCHITECTURE AND IMPLEMENTATION

We utilized a multiclass U-Net model to jointly segment the uterus and fetus in US images (see Figure 2). U-Net is a convolutional neural network consisting of an encoder path and a decoder path arranged as a U shape. In the

encoder path, spatial information decreases while feature representation information increases. In the decoder path, high-resolution features from the encoder path and spatial information are merged through a series of up-convolutions and concatenations operations. In our implemented model, the encoder path includes five layers that individually contain two 3×3 convolutions with rectified linear unit (ReLU) activation function, a 2×2 max pooling operator for downsampling, and a dropout operation with a rate of 0.1 to avoid overfitting. At the top layer, there are 8 feature channels, which are further downsampled and multiplied by two in each subsequent layer to reach 128 feature channels at the bottom layer. In the decoder path, the upsampling is performed using 2×2 up-convolutions. In each layer of the decoder, the result of upsampling is integrated with the
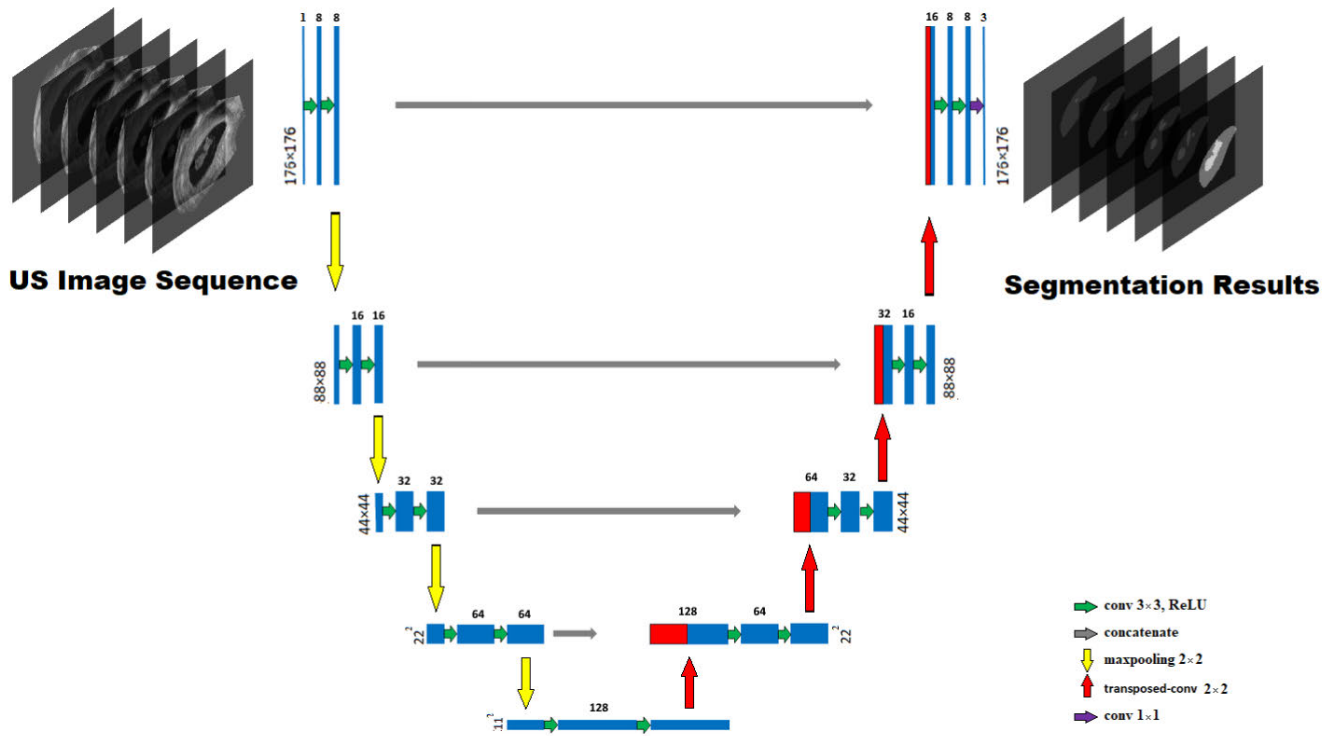
FIGURE 2. U-Net architecture [14]: the encoder path uses as input the US images, and the decoder path outputs the segmentation results.

cross-feature map of the encoder path, followed by two 3×3 convolutions with the ReLU activation function and a dropout operation with a rate of 0.1. In the final layer, a segmentation mask with the dimensions of the input image is generated by passing through a 1×1 convolution followed by a softmax activation function.

We implemented the U-Net model in Python with the Keras package using the TensorFlow back-end. The network is trained to optimize the pixel-wise categorical cross-entropy loss function defined as:

$$\text{Loss} = -\frac{1}{N}\sum_{n=1}^{N}\sum_{c=1}^{C}\big(y(n,c)\log p(n,c)\big) \tag{2}$$

where N is the number of image pixels, and C is the number of classes. For the considered images and fetus ages, we set $C = 3$ for three categories: fetus, uterus, and background. In Equation (2), $y(n,c) \in \{0,1\}$ is the reference segmentation, i.e. saying whether pixel n belongs or not to class c, and $p(n,c) \in (0,1)$ is the probability that pixel n belongs to class c, predicted by the network. Each pixel in a pixel-wise categorical cross-entropy loss function is considered an independent sample, and the average loss value over all pixels is used as the total loss for training. The Adam optimizer with a learning rate $\eta = 0.000001$, and 1000 epochs were employed for training the network. To save memory and computation resources, all the process is done on 2D slices. The results show a good consistency in 3D (which can be further improved using manual corrections if needed,

but this is rare with the final network). From the segmentation results, a 3D model is build.

C. GRAPHICAL USER INTERFACE
We developed a user-friendly GUI using the PyQt5 Python library to facilitate visualization and modification of the segmentation results (even by non experts in image analysis), illustrated in Figure 3 (see Appendix for details).

D. RESULTS OF SEGMENTATION AND 3D MODELING
The proposed method, with limited manual corrections needed, provided very good results, after visual evaluation and feedback from medical experts. Results corresponding to the images in Figure 1 are shown in Figure 4. A good agreement with the manual contours is observed.

It should be noted that the primary aim is to have realistic UFUs, hence a precise, pixel-wise evaluation is not required for the purpose of this study. Still the segmentation results are good, according to the reference manual segmentations, with a Dice score equal to 0.9 for the uterus, and equal to 0.8 for the fetus. Moreover, the potential imprecisions are much lower than the differences due to age, which thus allows for the subsequent study on the dependence on fetus age of SAR measures.

Due to the specificities of the electromagnetic characteristics of the amniotic field, including it in the model is important. Its small thickness makes it hardly visible in ultrasound images. Therefore, a systematic amniotic fluid
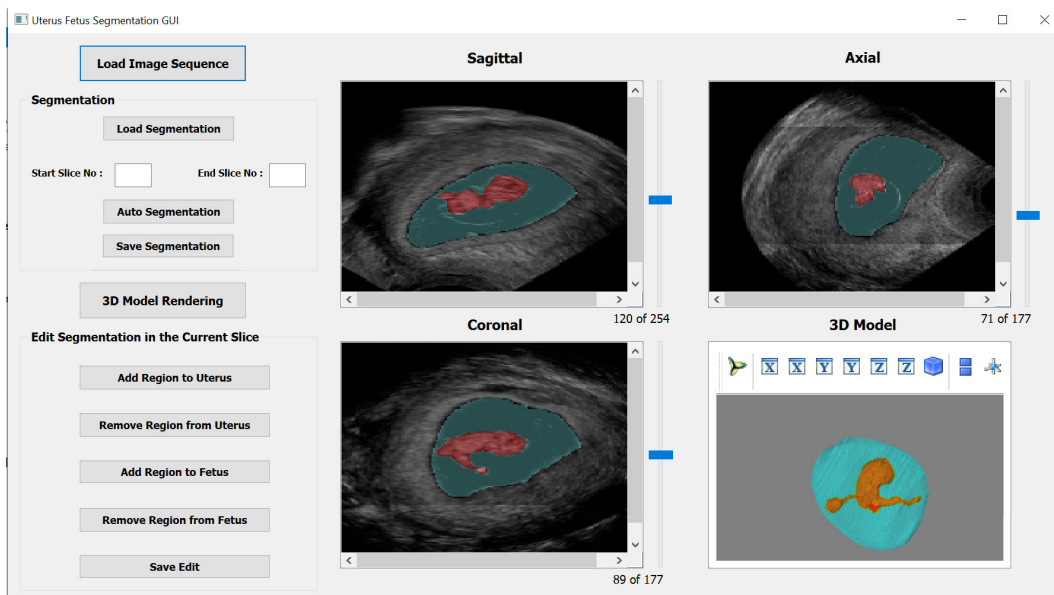
FIGURE 3. Graphical user interface for the segmentation of the uterus and fetus in ultrasound images. The left panel lists the functionalities offered to the user. On the right, the results of segmentation are illustrated on three orthogonal views, and the derived 3D model is shown. See the Appendix for details.
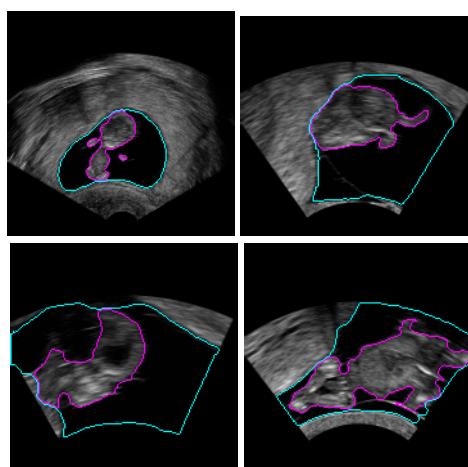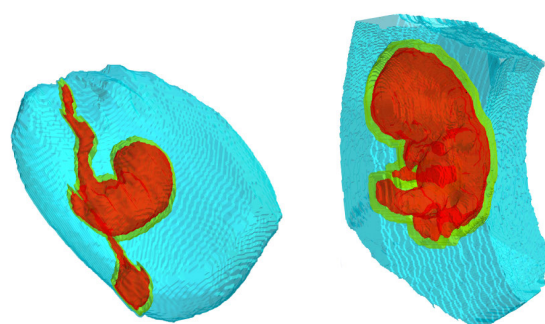

FIGURE 4. Examples of segmentation results on images not used for training. The uterus contours are displayed in blue and the fetus contours in magenta.

FIGURE 5. Examples of final 3D models, including the amniotic fluid layer (in green), for fetuses at 7 weeks.

layer was added around the fetus in all models, again with the aim of guaranteeing realism of the models. Based on medical expertise, a 2 mm thick layer is a realistic representation of the amniotic fluid, and this value was used in our experiments. Examples of final 3D models are displayed in Figure 5.

III. COMPUTATIONAL ELECTROMAGNETIC MODELING

The commercially available computational electromagnetic software CST MWS was used for whole body SAR calculations. A 26 year old human female voxel model called 'Ella' [24] was used for simulations. 'Ella' is composed of $265 \times 150 \times 840$ cubical voxels. The dimension of each voxel side is 2 mm. Each voxel is of a particular

tissue corresponding to the location of the voxel with in the human body. The frequency dependent, electromagnetic properties of human tissues are based on a five term Cole-Cole model [25]. 'Ella' is composed of 76 tissues.

Once the 'Ella' voxel model at the simulation frequency is generated, the UFU is inserted at the position of the uterus of the 'Ella'. This is done by altering the tissue (or material properties) of an 'Ella' voxel if it intersects with an UFU voxel. A picture of UFU inserted into the human model is shown in Figure 6. Even though both the computational electromagnetic and image segmentation output models are composed of cubical voxels, the sizes of these voxels are different. For the computational electromagnetic model, the voxel dimension is 2 mm. The dimension of the image segmentation output voxel is smaller, usually around 0.5 mm. Since the fetus is immersed in the amniotic fluid, it can undergo rotation. To study the effect of fetus rotation on SAR, a rotation of the UFU model can be applied by any
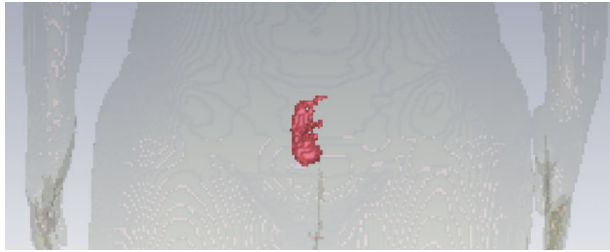
FIGURE 6. UFU model inserted into a human female model.

arbitrary rotation angles (three independent angles) before being inserted into the 'Ella' model.

The UFU is composed of three different tissues (or materials): uterus, amniotic fluid and fetus. The constitutive parameters (i.e. permittivity and conductivity) of these materials vary with frequency. The constitutive parameters of uterus of the UFU is the same as that of the uterus tissue in 'Ella'. The constitutive parameters of amniotic fluid is identical to that of Cerebrospinal Fluid (CSF) [9], which is available in the 'Ella' model. For the electromagnetic properties of the fetus, we have used the dielectric properties of rat fetus, which are provided in [26]. It is mentioned in [26] that there is no significant difference between dielectric properties of fetal homogenized tissue at different stages of pregnancy. Therefore, a unique value of permittivity and conductivity can be used for fetus at different stages of gestation. However, the permittivity and conductivity of the fetus is a function of frequency, which was taken into account in the simulations. The relative permittivity of the fetus at the frequencies of 1800 MHz, 2100 MHz, 2400 MHz, 2600 MHz, 3500 MHz are 55.71, 55.25, 54.80, 54.49, 53.09, respectively and the conductivities are 1.60 Sm^{-1}, 1.79 Sm^{-1}, 2.0 Sm^{-1}, 2.17 Sm^{-1}, 2.97 Sm^{-1}, respectively.

The human body has tissues with high relative permittivity. For instance, CSF has a relative permittivity of 65 at a frequency of 3.5 GHz. Therefore, discretization in numerical electromagnetic solver should be adequate (i.e. fine) to take this into consideration. The CST simulations were accelerated by using Graphical Processing Units (GPUs). Organ specific SAR was obtained by outputting the electric field values at discrete spatial points inside a box enclosing the UFU followed by the application of a discretized version of Equation (1). Let N_f be the number of 'Ella' computational electromagnetic voxels which make up the fetus and Δv be the volume of each voxel. For accurately calculating the fetus SAR, we divide each voxel into 8 sub-voxels. The fetus SAR can be estimated using

$$\text{Fetus SAR} \approx \frac{\frac{1}{2}\sigma_f \frac{\Delta v}{8} \sum_{i=1}^{N_f} \sum_{j=1}^{8} |\bar{E}_{ij}|^2}{\rho_f N_f \Delta v} \quad (3)$$

where σ_f, ρ_f are the fetus conductivity and fetus density, $\bar{E}_{ij}$ is the complex electric field intensity vector at the center of the jth sub-voxel with in the ith voxel.
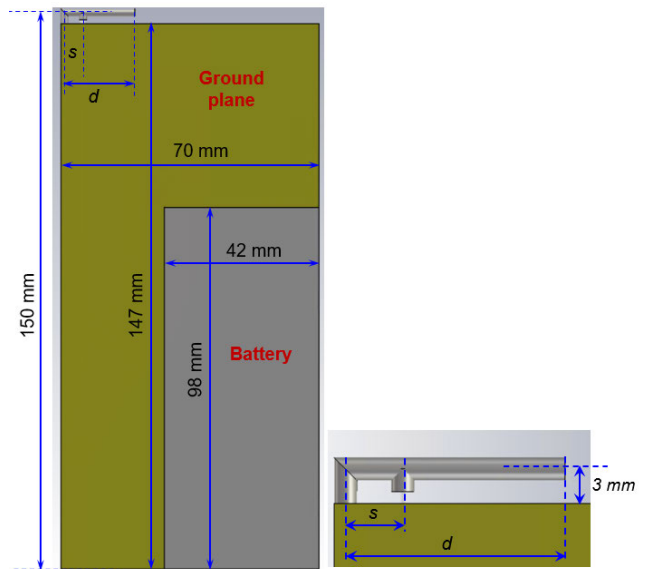

FIGURE 7. Generic Inverted F Antenna (IFA) with ground plane and battery. The ground plane thickness is 1 mm. The bent-feed separation is denoted by *s*, with *s* = 5 mm for all frequencies. The dimension *d* dictates the resonance frequency of the antenna. The figure on the right bottom shows an enlarged view of the bent monopole, its dimensions and the feed point. The radius of the monopole wire is 1 mm. Battery thickness is 2 mm and it is located above the ground plane.
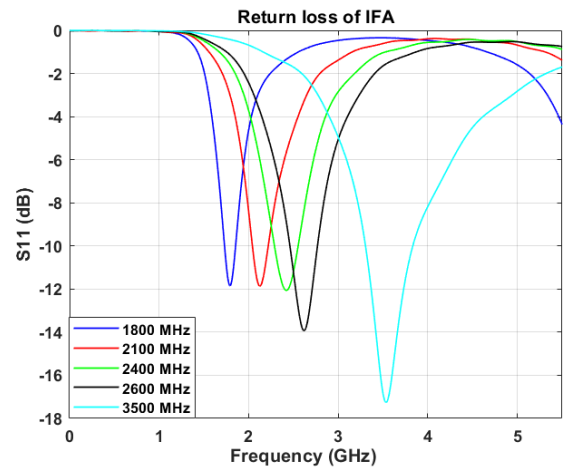
FIGURE 8. Return loss (dB) vs. frequency for IFAs designed to resonate at different frequencies.

IV. ANTENNAS
A. MOBILE PHONE ANTENNAS
We used Inverted-F Antennas (IFA) as the excitation source for the frequencies of 1800 MHz, 2100 MHz, 2400 MHz, 2600 MHz and 3500 MHz. IFA is a commonly used cell phone antenna [27]. The cell phone antenna used in the simulation is shown in Figure 7. The generic IFA consists of a bent monopole, ground plane and a battery. The large ground plane and metallic battery affect the radiation pattern significantly and hence it must be included for realistic SAR simulations. The dimensions of the ground plane and battery are similar to what is used in smart phones. All the components are made of Perfect Electric Conductor (PEC).
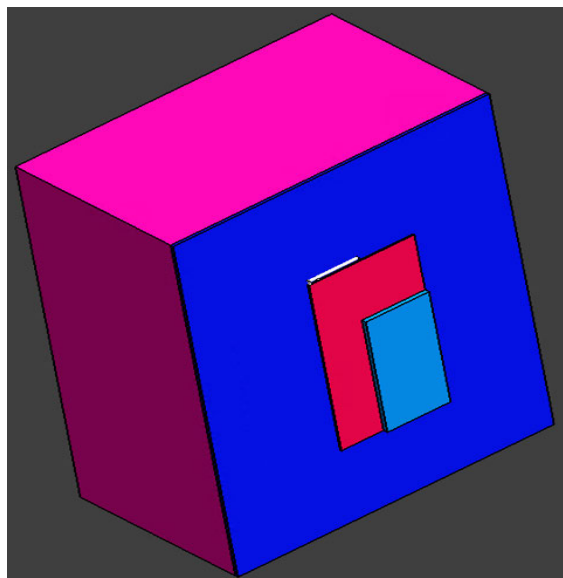
FIGURE 9. IFA over tissue emulating phantom. The tissue-equivalent phantom is pink colored and the phantom shell is in blue color. The lateral dimensions of the phantom are: 210 mm along the direction of phone width (i.e. 3 times the phone ground plane width) and 300 mm along the direction of phone height (i.e. 2 times the antenna ground plane height). The phantom has a thickness of 120 mm.

The resonant frequency of the antenna is dependent on the length of the bent monopole, i.e. $(d + 3)$ mm in Figure 7. The monopole lengths (i.e. $(d + 3)$ mm) for the antenna system to resonate at frequencies of 1800 MHz, 2100 MHz, 2400 MHz, 2600 MHz and 3500 MHz, are 38 mm, 33.5 mm, 31 mm, 29.85 mm and 19.15 mm, respectively. The return loss characteristics of the antennas designed at these frequencies are shown in Figure 8.

B. SAR ASSESSMENT PROCEDURE

It is a standard procedure in mobile phone SAR assessment experiments to calibrate the excitation antenna so that it induces 1 W/kg of peak spatial SAR averaged over 10 g [30] in a flat tissue-mimicking phantom [29]. A flat phantom of tissue-equivalent liquid covered with a thin shell of plastic is used to relate the peak spatial SAR averaged over 10 g in the lossy, tissue-equivalent liquid to the excitation voltage of the antenna [28]. The simulation setup for this procedure is depicted in Figure 9.

The FDTD solver of the Sim4Life platform v7.0.1 (ZMT Zurich MedTech AG, Switzerland) was used for these simulations. The main advantage of using Sim4Life platform is that it has specialized SAR post-processing features. The frequency dependent permittivity and conductivity of the tissue-equivalent liquid can be found in [29]. For the sake of reproducing the results, we have shown the relative permittivity and conductivity of the tissue-mimicking liquid in Table 1. The density of the tissue-equivalent liquid is 1000 kg/m^3. The plastic phantom shell thickness, phantom shell permittivity, phantom dimensions and the distance between the antenna and the phantom are all dependent on

TABLE 1. Tissue mimicking liquid properties and excitation voltage required to induce 1 W/kg peak spatial SAR averaged over 10 g in the liquid phantom.

Frequency (MHz)	Relative permittivity	Conductivity (S/m)	Antenna excitation (V)
1800	40.0	1.40	10.00
2100	39.8	1.49	8.74
2400	39.3	1.77	8.51
2600	39.0	1.96	8.63
3500	37.9	2.91	8.24
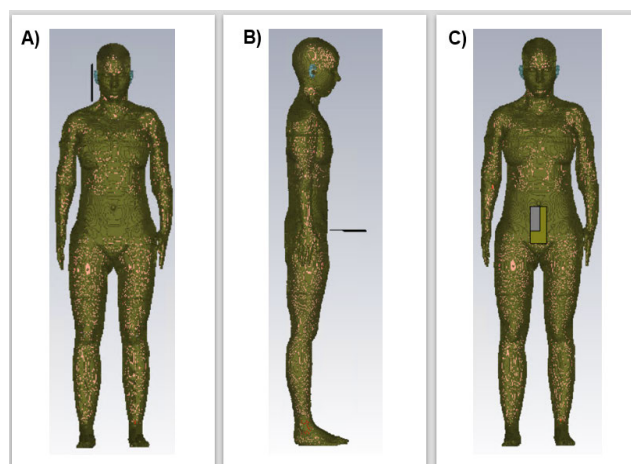
FIGURE 10. Phone antenna positions with respect to the human model. A) phone antenna near the ear, B) phone antenna near the belly and perpendicularly oriented to the body, and C) phone antenna near the belly with parallel orientation.

the frequency [29]. For all the frequencies we use in this work, the phantom shell thickness is 2 mm and the shell permittivity is 3.7. The antenna - phantom separation is 15 mm for all the frequencies. The lateral dimensions of the phantom are: 210 mm along the direction of phone width (i.e. 3 times the phone ground plane width) and 300 mm along the direction of phone height (i.e. 2 times the antenna ground plane height). The phantom has thickness of 120 mm. It was found that, at an excitation frequency of 1800 MHz, further increase in these phantom dimensions did not result in a change in the phantom SAR values. Since the wave attenuation increases with both frequency and conductivity (see Table 1), the phantom dimensions at 1800 MHz will be sufficient for the other higher frequencies. The antenna excitation voltage values required for the antenna displayed in Figure 7 to induce a SAR of 1 W/kg in the tissue phantom at different frequencies are listed in Table 1.

V. RESULTS AND DISCUSSION

The fetus SAR was estimated for a combination of three different phone positions [12], fetus ages and simulation frequencies. The antenna was excited with voltage sources which vary with frequency as shown in Table 1. The three phone positions (shown in Figure 10) are near the ear, near the belly and perpendicular to the body and near the belly and parallel to the body. The phone near the ear is the most

TABLE 2. Fetus SAR when the phone is near the ear.

Frequency (MHz)	7 week fetus SAR (μW/kg)	9 week fetus SAR (μW/kg)	11 week fetus SAR (μW/kg)
1800	6.49e-02	2.07e-01	1.38e-01
2100	6.76e-02	1.91e-01	1.25e-01
2400	1.65e-02	2.55e-02	1.93e-02
2600	3.89e-04	1.18e-02	1.02e-02
3500	6.81e-20	3.84e-14	6.47e-13

TABLE 3. Fetus SAR when the phone is near the belly with perpendicular orientation.

Frequency (MHz)	7 week fetus SAR (μW/kg)	9 week fetus SAR (μW/kg)	11 week fetus SAR (μW/kg)
1800	309.10	255.50	118.60
2100	98.69	90.06	36.23
2400	26.89	29.13	13.84
2600	12.82	15.50	10.14
3500	0.15	0.23	0.30

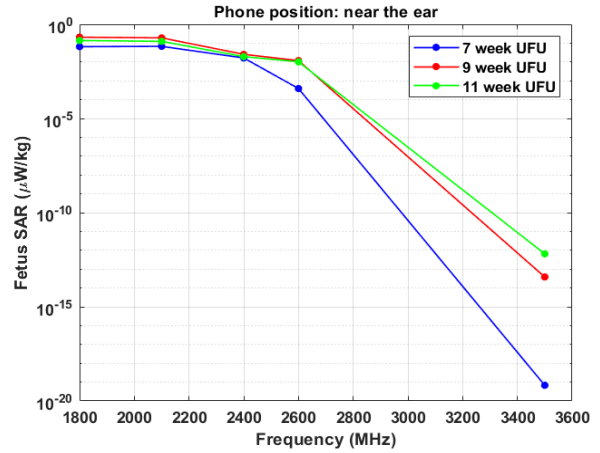**TABLE 4.** Fetus SAR when the phone is near the belly with parallel orientation.

Frequency (MHz)	7 week fetus SAR (μW/kg)	9 week fetus SAR (μW/kg)	11 week fetus SAR (μW/kg)
1800	374.90	291.57	260.47
2100	66.34	57.41	65.18
2400	13.33	13.41	22.41
2600	13.68	14.54	20.34
3500	0.29	0.43	0.53

commonly used position. We have included the other two positions (i.e. phone near the belly with different orientations) to estimate the worst case fetus exposure, when the phone is closer to the embryo.

The simulation used three fetuses of age 7 weeks, 9 weeks and 11 weeks, respectively. The three fetuses are not necessarily from the same person. The volumes of the 7 weeks, 9 weeks and 11 weeks old fetuses are 1392 mm^3, 6496 mm^3 and 12760 mm^3, respectively. The fetus SAR for the three phone positions and different frequencies are listed in Tables 2, 3 and 4. We have also plotted these values in Figures 11, 12 and 13 to visualize the general trend of these results.

As per ICNIRP 2020 [31], the maximum allowable whole body exposure level for general public is 80 mW/kg and the maximum allowable local exposure level for head and trunk is 2 W/kg. All the values in the tables are well below that limit. It should be reiterated that these SAR values are for mobile phones with excitation which induces 1 W/kg peak spatial SAR in tissue equivalent phantom, when it is located 15 mm from the phone. Since the SAR values are low, we did not perform bio-heat simulation to estimate temperature distribution.

From the data, it can be observed that the fetus SAR decreases with increasing frequency for all phone positions and fetus ages. This is the due to the fact that, at lower frequencies, the electromagnetic waves penetrate the tissues more than it penetrates at higher frequencies. The wave attenuation is proportional to the square root of frequency.

FIGURE 11. Fetus SAR (μW/kg) vs. frequency when the phone is near the ear.
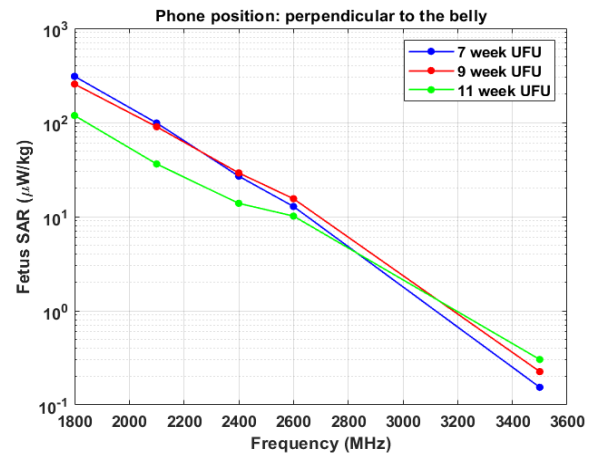
FIGURE 12. Fetus SAR (μW/kg) vs. frequency when the phone is near the belly with perpendicular orientation.
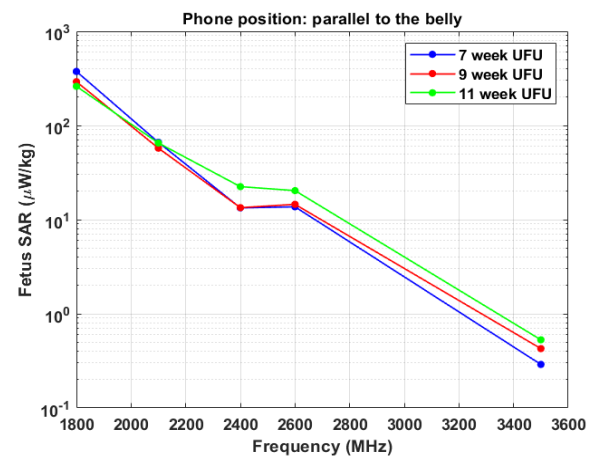
FIGURE 13. Fetus SAR (μW/kg) vs. frequency when the phone is near the belly with parallel orientation.

Another reason is that the wave attenuation is also proportional to the square root of conductivity and for most tissues, the conductivity increases with frequency. It can also be observed that the fetus SAR is very low, when the

phone is near the ear. Moreover at frequency of 3500 MHz, the fetus SAR is drastically reduced by several orders for all the phone positions and fetus ages. This is due to the RF energy being absorbed by skin and peripheral tissues.

A. EFFECT OF FETUS AGE AND ORIENTATION ON SAR

From Tables 2, 3 and 4, it can be observed that for a fixed phone position and frequency, the fetus SAR can either increase or decrease or vary randomly with respect to the fetus age. The fetus SAR is a function of several independent parameters such as the frequency of excitation, antenna (or phone) position and orientation, orientation of the fetus, fetus mass (or age), material properties of all the tissues of the body at a specific frequency, thickness of the amniotic fluid envelope and so on. For a fixed excitation frequency and phone position and orientation, the factors that affect SAR are the fetus mass (or age) and the fetus orientation. Even though the three fetuses are from a different person, the fetus volumes and hence their mass increase with age. Older fetus means more volume and hence more electromagnetic energy it absorbs, and therefore we would expect the SAR to be higher. However, the mass of the fetus also increases with age. The rate of increase of absorbed EM energy with respect to fetus age may be smaller or higher than that rate of increase in mass with fetus age. To exemplify, consider the case of a lossy, dielectric sphere illuminated by a plane, electromagnetic wave. When the sphere radius is much larger than the wavelength (i.e. geometrical optics regime), the absorption cross-section is proportional to R^2, where R is the radius of the sphere [32]. Therefore, the power absorbed is proportional to R^2. However, the sphere mass is proportional to R^3. Consequentially, the sphere SAR is linearly proportional to $1/R$. This simple result is for a spherical object and a plane wave. In our case, we have an irregularly scattering object embedded inside a very complex, inhomogeneous human body, and the incident wave is no longer a simple plane wave. Therefore, we cannot always qualitatively predict the fetus SAR trend with respect to its age.

Another major factor is the fetus orientation. For the SAR results we have presented, the three fetuses aged 7 weeks, 9 weeks and 11 weeks are not all in the same orientation. The image segmentation model was embedded into the computational electromagnetic model without changing the orientation. This is acceptable in the sense that the fetus can randomly undergo rotational transformation in the amniotic fluid. Let us say our reference coordinate frame has z direction along the human body's height and x, y directions in a plane orthogonal to the height direction. In order to show the variation of fetus SAR with respect to orientation angle, we varied the orientation of the fetus with respect to z direction from 0 to 360 degrees for the three fetuses. The fetus SAR variation with respect to this orientation at frequency of 1800 MHz and when phone near the belly in perpendicular direction is shown in Figure 14.
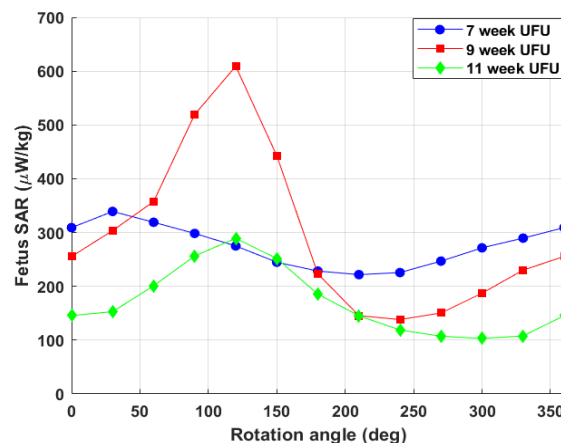
FIGURE 14. Fetus SAR vs. rotation angle for fetuses of different ages. Simulation frequency is 1800 MHz and the phone is near the belly and perpendicularly oriented to body.

This figure shows that the maximum SAR of nearly 0.6 mW/kg is well below the ICNIRP restriction of 80 mW/kg. A more thorough approach to evaluate the SAR variation with respect to fetus orientation is to use stochastic dosimetric techniques such as Polynomial Chaos Expansion (PCE) [1]. In PCE, SAR is approximated as a function of several independent parameters (fetus orientation angles in our case), by using SAR simulation outputs at a fixed number of points in the independent variable domain space. This is done by using orthogonal basis functions such as Legendre polynomials. We attempted PCE for the problem of fetus SAR variation with respect to three fetus orientation angles. However, we were not able to obtain good convergence. The total time required for embedding the image segmentation output into the computational electromagnetic model and further SAR simulation at a fixed set of orientation angles was more than one hour. Since a large number of points are required for PCE convergence in the three dimensional independent variable space, the time required to build a PCE model was prohibitively large. In Figure 14, it can be seen that at different orientation angles, the fetus SAR can vary randomly with age. Even though in general the trend is 7 week fetus SAR greater than 9 week fetus SAR which in turn is greater 11 week fetus SAR, at certain angles of rotation (for example 100 degrees), this order is violated. This random variation of the fetus SAR with respect to fetus orientation and fetus mass explains the somewhat unpredictable dependence of fetus SAR with respect to fetus age as seen in Tables 2, 3 and 4, and Figures 11, 12 and 13.

B. SAR IN UTERUS OF VOLUME EQUAL TO FETUS

The processing time for inserting image segmented UFU into the 'Ella' human model followed by full wave electromagnetic simulation is more than one hour. This is in addition to the time and effort for image segmentation of the ultrasound images. In order to circumvent this series of steps, we try to verify whether SAR in uterus tissue of same volume

TABLE 5. Fetus SAR vs. equivalent volume uterus SAR for a 7 week UFU. Phone position is near the belly with perpendicular orientation.

Frequency (MHz)	7 week fetus SAR (μW/kg)	Equivalent volume uterus SAR (μW/kg)
1800	309.10	346.80
2100	98.69	86.68
2400	26.89	29.09
2600	12.82	13.52
3500	0.15	0.12

TABLE 6. Fetus SAR vs. equivalent volume uterus SAR for a 9 week UFU. Phone position is near the belly with perpendicular orientation.

Frequency (MHz)	9 week fetus SAR (μW/kg)	Equivalent volume uterus SAR (μW/kg)
1800	255.50	352.70
2100	90.06	94.11
2400	29.13	37.83
2600	15.50	19.75
3500	0.23	0.24

TABLE 7. Fetus SAR vs. equivalent volume uterus SAR for a 11 week UFU. Phone position is near the belly with perpendicular orientation.

Frequency (MHz)	11 week fetus SAR (μW/kg)	Equivalent volume uterus SAR (μW/kg)
1800	118.60	169.70
2100	36.23	40.49
2400	13.84	18.69
2600	10.14	13.56
3500	0.30	0.36

and shape as that of fetus plus amniotic fluid envelope can approximate the fetus SAR. The equivalent uterus tissue mass is at the same location as that of the fetus.

The fetus and amniotic fluid voxels of the UFU are replaced with uterus tissue voxels. Fetus SAR compared with the equivalent volume uterus SAR for the three different UFU ages are listed in Tables 5, 6, and 7. For all the three UFU ages and frequencies, it can be noticed that the uterus SAR is only marginally different from that of the fetus SAR. Moreover, the equivalent volume uterus SAR is always higher than that of fetus SAR. This is due to the electromagnetic shielding effect caused by the surrounding amniotic fluid. Since similar values of SAR were obtained for both the fetus and an equivalent volume of uterus, we conclude that for young fetuses, we can obtain a good estimate of the fetus SAR by just calculating the SAR in uterus tissues of same volume. This result is advantageous because image segmentation of ultrasound images followed by insertion of the model into a human body model is cumbersome.

VI. CONCLUSION

In this work, we proposed and developed a deep-learning based image segmentation method to build realistic digital 3D models of uterus fetus units from ultrasound images. The results were in good agreement with the reference manual segmentation. The aim of this study was to have a realistic model of the fetus, and the good Dice values (0.9 for the

uterus and 0.8 for the fetus) indicated that the segmentation results were sufficient for the subsequent steps. The potential imprecision on the segmentation did not have a significant impact on the numerical simulations. What is important is to have realistic differences according to fetus age, that we were indeed able to obtain.

The image segmented 3D UFU model was embedded inside a computational electromagnetic model of a human body, allowing for the numerical estimation of fetus SAR for a combination of commonly used cellular phone frequencies, phones positions and fetus ages. Fetus SAR values were found to be well below the ICNIRP prescribed limit for all the cases. We also examined and inferred the effects of fetus age and fetus orientation on fetus SAR. In general, the fetus SAR displays a random variation with respect to both of these parameters. We further calculated the SAR in a mass of uterus which is centered at the embryo's location and whose volume is equivalent to that of the embryo. The uterus SAR values were comparable to the fetus SAR values and can be used in epidemiological studies to analyze the possible impact of RF-EMF at early stages of gestation.

In future work, fetus from the ultrasound images could be differentiated into individual tissues such as brain, muscle, etc. Ultrasound images are also still improving, which may result in much smoother and more accurate SAR predictions. The series of procedures proposed in this paper will be used as guideline for future work.

APPENDIX

This appendix provides some more details about the GUI developed to facilitate visualization and modification of the segmentation results. As shown in Figure 3, the proposed GUI comprises five main parts: Load Image Sequence, Segmentation, 3D Model Rendering, Edit Segmentation in the Current Slice, and 4 Display Windows. When the **Load Image Sequence** push button is clicked, a file selection window is opened. Then, the user can choose a sequence of US images displayed in three display windows: sagittal, axial, and coronal slices. In the **Segmentation** part, when segmentation results are available for the current US sequence, the user can load them by pressing the **Load Segmentation** push button and selecting the folder in which the results are stored. Following that, the segmentation results of the uterus and the fetus are displayed as an overlay on the original images. To utilize the proposed automatic segmentation method, first, the user must determine the slices within a given sequence that need to be segmented by selecting **Start Slice No** and **End Slice No** in two relevant edit boxes. By clicking on the **Auto Segmentation** push button, the trained U-Net model introduced earlier in the section will automatically segment determined slices and show the results as an overlay on the original slices in the three display windows. Following segmentation, using the **3D Model Rendering** push button, a three-dimensional model of the uterus and the fetus is created, and displayed in the 4th display window entitled **3D Model**. It is possible for

the user to manually modify the obtained segmentation at any time by using **Edit Segmentation in the Current Slice** part of the GUI. Four push buttons are available in this part of the interface for adding or removing regions from the uterus or fetus. Each push button opens an editing window that allows the user to increase or eliminate regions from the segmentation result. Finally, the **Save Segmentation** or **Save Edit** push buttons can be applied to save the results.

ACKNOWLEDGMENT

REFERENCES

[1] J. Wiart, *Frequency Human Exposure Assessment: From Deterministic to Stochastic Methods*. Hoboken, NJ, USA: Wiley, 2016.

[2] M. A. Jamshed, F. Héliot, and T. W. C. Brown, "A survey on electromagnetic risk assessment and evaluation mechanism for future wireless communication systems," *IEEE J. Electromagn., RF Microw. Med. Biol.*, vol. 4, no. 1, pp. 24–36, Mar. 2020.

[3] M. Bonato, L. Dossi, S. Gallucci, M. Benini, G. Tognola, and M. Parazzini, "Assessment of human exposure levels due to mobile phone antennas in 5G networks," *Int. J. Environ. Res. Public Health*, vol. 19, no. 3, p. 1546, Jan. 2022.

[4] E. Chiaramello, M. Parazzini, S. Fiocchi, P. Ravazzani, and J. Wiart, "Assessment of fetal exposure to 4G LTE tablet in realistic scenarios: Effect of position, gestational age, and frequency," *IEEE J. Electromagn., RF Microw. Med. Biol.*, vol. 1, no. 1, pp. 26–33, Jun. 2017, doi: 10.1109/JERM.2017.2727279.

[5] T. Nagaoka, T. Togashi, K. Saito, M. Takahashi, K. Ito, and S. Watanabe, "An anatomically realistic whole-body pregnant-woman model and specific absorption rates for pregnant-woman exposure to electromagnetic plane waves from 10 MHz to 2 GHz," *Phys. Med. Biol.*, vol. 52, no. 22, pp. 6731–6745, Nov. 2007.

[6] H. Kawai, T. Nagaoka, S. Watanabe, K. Saito, M. Takahashi, and K. Ito, "Computational dosimetry in embryos exposed to electromagnetic plane waves over the frequency range of 10 MHz–1.5 GHz," *Phys. Med. Biol.*, vol. 55, no. 1, pp. N1–N11, Jan. 2010.

[7] N. Varsier, S. Dahdouh, A. Serrurier, J.-P. De la Plata, J. Anquez, E. D. Angelini, I. Bloch, and J. Wiart, "Influence of pregnancy stage and fetus position on the whole-body and local exposure of the fetus to RF-EMF," *Phys. Med. Biol.*, vol. 59, no. 17, pp. 4913–4926, Sep. 2014.

[8] A. Razjouyan, *Biomed. Phys. Eng. Exp.*, vol. 4, no. 4, 2018, Art. no. 045032.

[9] J. W. Hand, Y. Li, E. L. Thomas, M. A. Rutherford, and J. V. Hajnal, "Prediction of specific absorption rate in mother and fetus associated with MRI examinations during pregnancy," *Magn. Reson. Med.*, vol. 55, no. 4, pp. 883–893, Apr. 2006.

[10] J. W. Hand, Y. Li, and J. V. Hajnal, "Numerical study of RF exposure and the resulting temperature rise in the foetus during a magnetic resonance procedure," *Phys. Med. Biol.*, vol. 55, no. 4, pp. 913–930, Feb. 2010.

[11] S. Kikuchi, K. Saito, M. Takahashi, and K. Ito, "Temperature elevation in the fetus from electromagnetic exposure during magnetic resonance imaging," *Phys. Med. Biol.*, vol. 55, no. 8, pp. 2411–2426, Apr. 2010.

[12] R. Takei, T. Nagaoka, K. Saito, S. Watanabe, and M. Takahashi, "SAR variation due to exposure from a smartphone held at various positions near the torso," *IEEE Trans. Electromagn. Compat.*, vol. 59, no. 2, pp. 747–753, Apr. 2017.

[13] E. van Deventer, E. van Rongen, and R. Saunders, "WHO research agenda for radiofrequency fields," *Bioelectromagnetics*, vol. 32, no. 5, pp. 417–421, Jul. 2011.

[14] O. Ronneberger, P. Fischer, and T. Brox, "U-Net: Convolutional networks for biomedical image segmentation," in *Proc. Med. Image Comput. Comput.-Assist. Intervent. (MICCAI)*, 2015, pp. 234–241.

[15] G. Du, X. Cao, J. Liang, X. Chen, and Y. Zhan, "Medical image segmentation based on U-net: A review," *J. Imag. Sci. Technol.*, vol. 64, no. 2, 2020, Art. no. 020508.

[16] N. Siddique, S. Paheding, C. P. Elkin, and V. Devabhaktuni, "U-net and its variants for medical image segmentation: A review of theory and applications," *IEEE Access*, vol. 9, pp. 82031–82057, 2021.

[17] X. X. Yin, L. Sun, Y. Fu, R. Lu, and Y. Zhang, "U-net-based medical image segmentation," *J. Healthcare Eng.*, vol. 2022, Apr. 2022, Art. no. 4189781.

[18] M. Amiri, R. Brooks, and H. Rivaz, "Fine-tuning U-net for ultrasound image segmentation: Different layers, different outcomes," *IEEE Trans. Ultrason., Ferroelectr., Freq. Control*, vol. 67, no. 12, pp. 2510–2518, Dec. 2020.

[19] M. Amiri, R. Brooks, B. Behboodi, and H. Rivaz, "Two-stage ultrasound image segmentation using U-Net and test time augmentation," *Int. J. Comput. Assist. Radiol. Surgery*, vol. 15, no. 6, pp. 981–988, Jun. 2020.

[20] V. B. Shereena and G. Raju, "Medical ultrasound image segmentation using U-Net architecture," in *Proc. Commun. Comput. Inf. Sci.*, vol. 1613, 2022, pp. 361–372.

[21] D. Qiao and F. Zulkernine, "Dilated squeeze-and-excitation U-net for fetal ultrasound image segmentation," in *Proc. IEEE Conf. Comput. Intell. Bioinf. Comput. Biol. (CIBCB)*, Oct. 2020, pp. 1–7.

[22] V. Ashkani Chenarlogh, M. Ghelich Oghli, A. Shabanzadeh, N. Sirjani, A. Akhavan, I. Shiri, H. Arabi, M. Sanei Taheri, and M. K. Tarzamni, "Fast and accurate U-net model for fetal ultrasound image segmentation," *Ultrason. Imag.*, vol. 44, no. 1, pp. 25–38, Jan. 2022.

[23] V. Nagabotu and A. Namburu, "Precise segmentation of fetal head in ultrasound images using improved U-net model," *ETRI J.*, pp. 1–12, Jul. 2023, doi: 10.4218/etrij.2023-0057.

[24] ITIS Foundation. *Human Models*. Accessed: Sep. 2022. [Online]. Available: https://itis.swiss/virtual-population/virtual-population/vip3/ella/

[25] S. Gabriel, R. W. Lau, and C. Gabriel, "The dielectric properties of biological tissues: III. Parametric models for the dielectric spectrum of tissues," *Phys. Med. Biol.*, vol. 41, no. 11, pp. 2271–2293, Nov. 1996.

[26] A. Peyman and C. Gabriel, "Dielectric properties of rat embryo and foetus as a function of gestation," *Phys. Med. Biol.*, vol. 57, no. 8, pp. 2103–2116, Apr. 2012.

[27] Z. Zhang, *Antenna Design for Mobile Devices*. Hoboken, NJ, USA: Wiley-IEEE Press, 2017, pp. 138–159.

[28] T. Onishi and S. Uebayashi, "Influence of phantom shell on SAR measurement in 3–6 GHz frequency range," *IEICE Trans. Commun.*, vol. 88, no. 8, pp. 3257–3262, 2005.

[29] *Measurement Procedure for the Assessment of Specific Absorption Rate of Human Exposure to Radio Frequency Fields From Hand-Held and Body-Mounted Wireless Communication Devices*, document IEC 62209-1, 2016.

[30] J. Grund, K.-U. Rathjen, C. Rädel, M. Stiemer, and S. Dickmann, "Planar multilayer model of human tissue exposed to a plane electromagnetic wave," *IEEE J. Electromagn., RF Microw. Med. Biol.*, vol. 5, no. 4, pp. 305–312, Dec. 2021.

[31] International Commission on Non-Ionizing Radiation Protetion (ICNIRP), "ICNIRP guidelines for limiting exposure to time-varying electric, magnetic, and electromagnetic fields (up to 300 GHz)," *Health Phys.*, vol. 118, no. 5, pp. 483–524, Mar. 2020.

[32] C. F. Bohren and D. R. Huffman, *Absorption and Scattering of Light by Small Particles*. Hoboken, NJ, USA: Wiley, 1998.

SRIKUMAR SANDEEP received the M.S. and Ph.D. degrees in electrical engineering from the University of Colorado, Boulder, in 2011 and 2012 respectively. He was a Postdoctoral Researcher with the University of Colorado, in 2013, focusing on antenna design and with École Polytechnique, Montreal, in 2016, where he involved on metasurfaces. This was followed by research scientist appointments with Singapore University of Technology and Design (SUTD), Norwegian University of Science and Technology (NTNU), and Télécom Paris. His technical interests include computational electromagnetics, antenna design, metasurfaces, signal integrity, wireless power transfer, high performance computing, bioelectromagnetics, and applied machine learning. He is an expert in finite difference time domain (FDTD) method and method of moments (MoM). He has authored more than 20 publications and is a co-inventor of a U.S. patent. In addition to academic experience, he has more than four years of industrial experience in software development, electronics engineering, and signal integrity at several companies, including Qualcomm Inc., and Trimble Navigation.

ALIREZA VARD received the B.Sc. degree in software engineering from the University of Isfahan, in 2004, and the M.Sc. and Ph.D. degrees in computer engineering from the University of Isfahan, in 2007 and 2012, respectively. He was a Postdoctoral Researcher specializing in medical image processing with Télécom Paris, in 2019. He was a Visiting Researcher with the Biomedical Imaging Group Rotterdam, Erasmus University Medical Centre, and the Chair of the Computer Aided Medical Procedures and Augmented Reality, Technical University of Munich (TUM), in 2016 and 2018, respectively. He was a Senior Researcher with IMAGES and C2M teams, Télécom Paris, in 2022. He is currently an Associate Professor with the Department of Biomedical Engineering, Isfahan University of Medical Sciences (IUMS). His research interests include medical image processing, machine learning, deep learning, design, and development of medical image processing software tools.

ISABELLE BLOCH received the degree from École des Mines de Paris, Paris, France, in 1986, and the master's degree from the University Paris 12, Paris, in 1987, the Ph.D. degree from Ecole Nationale Supérieure des Télécommunications (Télécom Paris), Paris, in 1990, and the Habilitation degree from University Paris 5, Paris, in 1995. She has been a Professor with Télécom Paris until 2020. She is currently a Professor with Sorbonne Université. Her current research interests include 3-D image understanding, computer vision, mathematical morphology, information fusion, fuzzy set theory, structural, graph-based, and knowledge-based object recognition, spatial reasoning, hybrid and explainable artificial intelligence, and medical imaging.

MÒNICA GUXENS is currently a Research Professor and the Head of the BrainChild Laboratory, Barcelona Institute for Global Health (ISGlobal). She is the Director of Spanish INMA Project, a multi-site birth cohort. She has been leading several projects in RF-EMF and health. She is also coordinating the Horizon Europe Project GOLIAT ''5G exposure, casual effects, and risk perception through citizen engagement.'' Her research interests include environmental factors, including electromagnetic fields, on children's development, in particular on brain development.

JOE WIART (Senior Member, IEEE) received the Diploma degree in telecommunication engineering, in 1992, the Ph.D. degree, in 1995, and the HDR degree, in 2015. Since 2015, he has been the holder of the Chair C2M Caractérisation, modélisation et maitrise, Institut Mines Telecom, Telecom Paris. His works gave rise to more than 150 publications in journals and more than 200 communications. His research interests include experimental, numerical methods, machine learning, and statistics applied in electromagnetism, dosimetry, and exposure monitoring. He has been an Emeritus Member of the Society of Electrical Engineers (SEE), since 2008. He is also the Chairperson of the TC106x of the European Committee for Electrotechnical Standardization (CENELEC) in charge of EMF exposure standards. He was the past Chairperson of the International Union of Radio Science (URSI) Commission K and has been the Chairperson of the French Chapter of URSI.

● ● ●